Chapter 4. Beam Dynamics

4.1. Space charge and beam stability

J. Holmes, K.Y. Ng, C. Prior

4.1.1. Tune shifts

The *betatron tunes* ν_z, $z = x$ or y, of transverse oscillations of charged particles in the beam moving with axial velocity $v = \beta c$, c being the velocity of light, are mainly determined by the applied focusing forces due to quadrupoles. With finite beam current the tunes are shifted, both by direct space charge and by image forces due to induced voltages in the surrounding structure impedances. At relativistic beam energies, the space charge forces are strongly reduced by a factor $\gamma^{-2} = 1 - \beta^2$ due to partial compensation of electric and magnetic forces. However, in the PD2 at 600 MeV injection energy, $\gamma = 1.640$ and the space charge term is largely dominant.

The *coherent* and *incoherent tune shifts* of a beam with half width a_x and half height a_y consisting of N_p protons are [1]

$$\Delta\nu_{\mathrm{coh},z} = -\frac{N_p r_p R}{\pi\nu_z\gamma\beta^2}\left[\left(\frac{1}{\gamma^2 B_f}+\beta^2\right)\frac{\xi_{1z}}{h^2} + \beta^2\frac{\epsilon_{1z}}{h^2} + \mathcal{F}\beta^2\frac{\epsilon_{2z}}{g^2}\right], \tag{4.1}$$

$$\Delta\nu_{\mathrm{incoh},z} = -\frac{N_p r_p R}{\pi\nu_z\gamma\beta^2}\left[\left(\frac{1}{\gamma^2 B_f}+\beta^2\right)\frac{\epsilon_{1z}}{h^2} + \beta^2\frac{\epsilon_{1z}}{h^2} + \mathcal{F}\beta^2\frac{\epsilon_{2z}}{g^2} + \frac{2\epsilon_{\mathrm{spch},z}}{\gamma^2 a_y(a_x+a_y)B_f}\right]. \tag{4.2}$$

where r_p is the classical radius, B_f is the bunching factor, and R is the mean radius of the accelerator ring. The *coherent Laslett image coefficients* $\xi_{1,2z}$ and *incoherent Laslett image coefficients* $\epsilon_{1,2z}$ describe the strength of image forces for a particular geometry. For a rectangular vacuum chamber of total height $2h = 4$ in and width $2w = 6$ in, the images coefficients are $\xi_{1x} = 0.0887$, $\xi_{1y} = 0.5737$, $\epsilon_{1x} = -\epsilon_{1y} = -0.1617$. For the magnet pole gaps, the geometry of two infinite plates separated by $2g = 4$ in covering $\mathcal{F} = 0.5$ of the ring is assumed, giving $\epsilon_{2x} = \epsilon_{2y} = -\pi^2/24$. Because of multi-turn injection, a uniform distribution in the transverse directions is assumed for the self-field in the last term in Eq. (4.2), giving the space charge coefficients $\epsilon_{\mathrm{spch},y} = a_y/(a_x+a_y)$ and $\epsilon_{\mathrm{spch},x} = a_y^2/[a_x(a_x+a_y)]$. The tune shifts are calculated at every moment of the ramp cycle and are plotted in Fig. 4.1. In the computation, the standard rf voltage table has been used, which assumes a fixed bucket area in the latter part of the ramp 20.3 ms into the cycle. The bunching factor B_f is computed from the bunch area which is assumed to increase linearly from 0.05 eV-s just after injection to 0.15 eV-s at extraction. The beam radii are computed from the 95% normalized emittance $\epsilon_{N95\%} = 40 \times 10^{-6}$ πm. We see that the bunching factor, which is also plotted in a different scale, decreases rapidly as the beam is captured into the rf bucket adiabatically. As a result, the tune shifts assume their maximal values

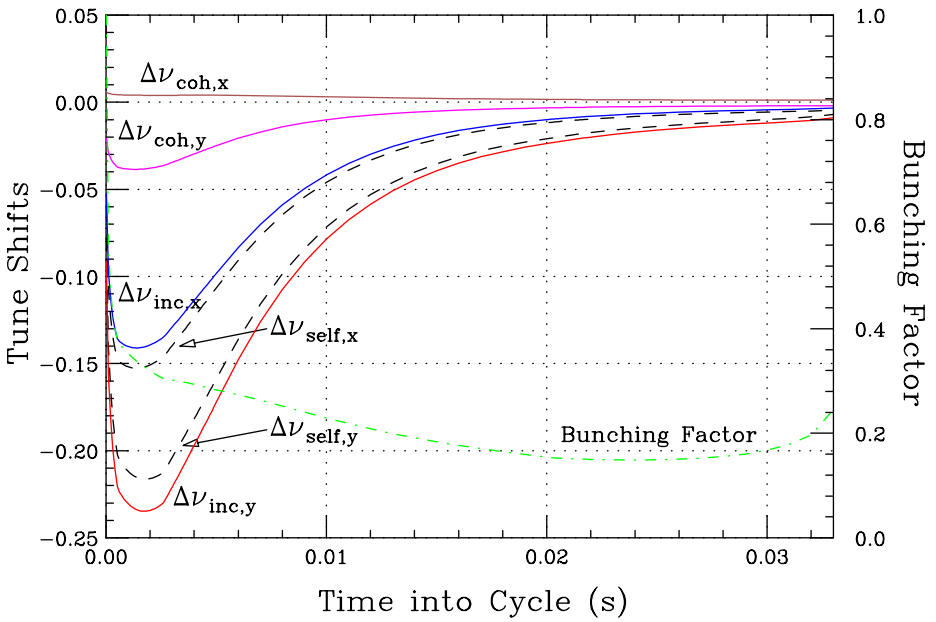

Figure 4.1. (color) Coherent and incoherent betatron tune shifts of the PD2.

about 8 ms into the cycle. The coherent tune shifts come from images in the vacuum wall and they are small. The incoherent tune shifts are dominated by the self-field contributions which are denoted by $\nu_{\mathrm{self},x}$ and $\nu_{\mathrm{self},y}$ in the figure. At their maximal values, we can write

$$\Delta\nu_{\mathrm{incoh},x} = -0.153 + 0.013 = -0.140\,, \quad \Delta\nu_{\mathrm{incoh},y} = -0.216 - 0.018 = -0.234\,, \qquad (4.3)$$

where the first term in the middle corresponds to self-force contributions and the second term to image contributions. It is obvious that space charge dominates the incoherent tune shifts. However, it is well-known that only the coherent tune shifts are responsible for parametric resonances [2]. Although the space charge self-force does not contribute to the dipole coherent tune shifts, it contributes to the quadrupole coherent tune shifts. The symmetric coherent quadrupole mode will be shifted by $2 \times \frac{3}{4}$ of the incoherent dipole shift, or $\nu_{\mathrm{quad}} = 2\left[\nu_{\mathrm{dipole}} - \frac{3}{4}|\Delta\nu_{\mathrm{incoh}}|\right]$. Therefore, $2\nu_y$ is shifted from 2×7.34 to 2×7.16 and $2\nu_x$ is shifted from 2×11.70 to 2×11.61. With the vertical and horizontal betatron bare tunes at $\nu_{y0} = 7.34$ and $\nu_{x0} = 11.7$, the equivalent vertical tune ν_y passes through the stopbands at 7.33, 7.25 and 7.20, while the equivalent horizontal tune ν_x passes through the stopband at 11.67.

4.1.2. Space charge at Injection

The code TRACK-2D, developed in the Rutherford Laboratory in England [3], also includes transverse space-charge effects, making use of a nonlinear space-charge solver based on finite elements. The code has been applied to the parameters of the Proton Driver to study the evolution of particles in transverse phase space. The results are shown in Figs. 4.2 for the transverse plane (x, y). Reading from left to right and top to bottom, each plot shows a sequence of shots in the first 1, 5, 10, 15, 20, 25, 30, 35, 40, 45, and 51 revolutions. Al-

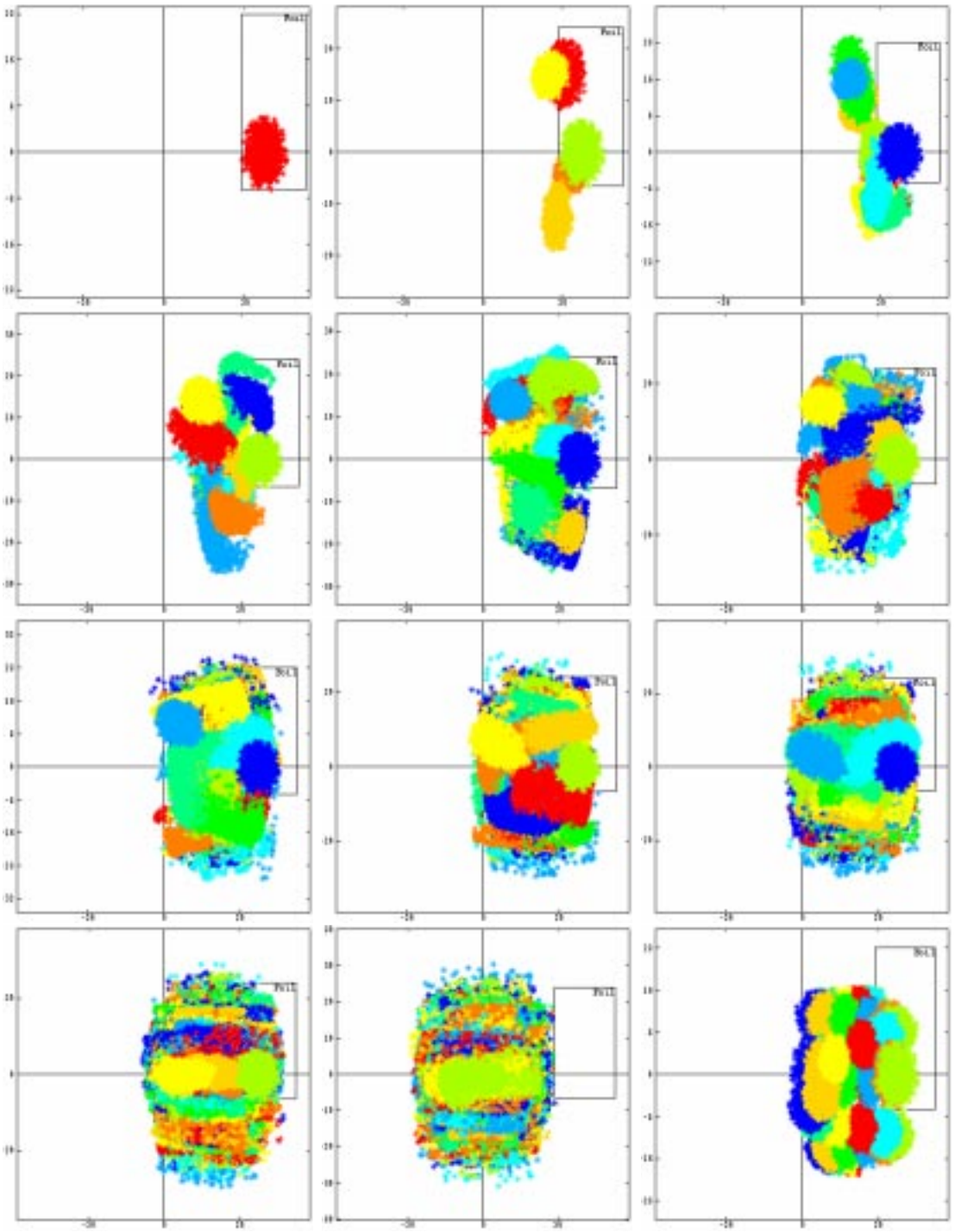

Figure 4.2. (color) Reading from left to right and top to bottom are x-y plots of the injection beam cross sections at stripping foil at the 1, 5, 10, 15, 20, 25, 30, 35, 40, 45, and 51 revolutions with the space charge force implemented. The last plot is at the 51 revolutions with the space charge force turned off. Note that the plots are on different scale. However, the stripping foil, depicted as a rectangle, should be of the same physical size.

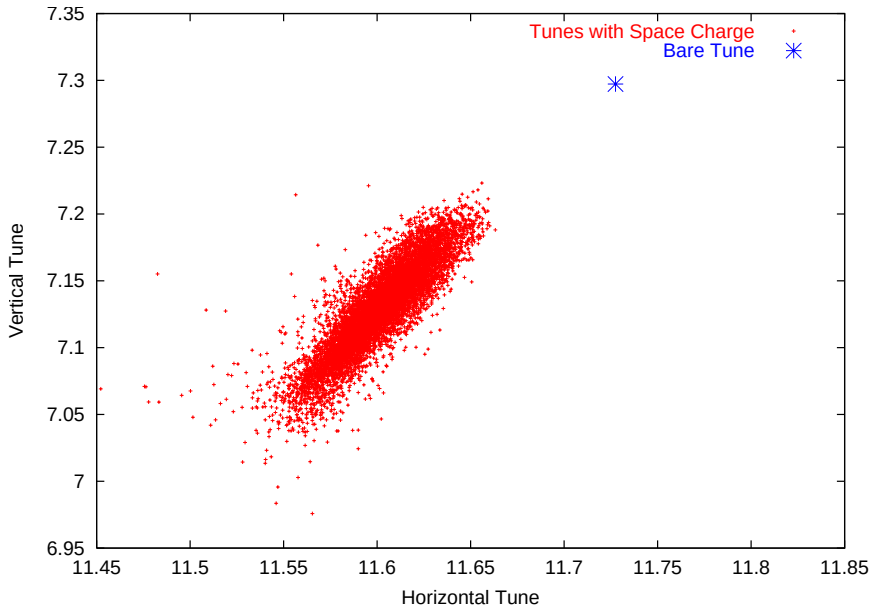

Figure 4.3. Tune foot-print after injection, showing the tunes of individual particles shifted by the space charge self-force from the bare values.

though these plots are on different scales, the transverse size of the injected beam can be inferred by comparison with the size of the stripping foil, which is depicted as a rectangle in every plot. The last plot is at the 51 revolutions with the space charge force turned off. It is clear by comparing this plot with the second last one that space charge does blow up the beam size.

A simulation of the injection was also performed with the transverse space charge force fully taken into account to determine the transverse locations of the beam particles [4]. The injection painting scheme follows the description in Sec. 7.1. Figure 4.3 shows the betatron foot-print just after injection. We see that the tunes are shifted from the bare values of $\nu_{y0} = 7.34$ and $\nu_{x0} = 11.7$ to the foot print that has the spreads of $\Delta\nu_y \sim 0.15$ and $\Delta\nu_x \sim 0.10$. The amounts of shifts closely resemble what were predicted in Fig. 4.1. In Fig. 4.4, the fractional number of particles that have exceeded a certain normalized emittance. For example, only $\sim 5\%$ full outside 30×10^{-6} πm, and this number becomes negligibly small at 40×10^{-6} πm.

4.1.3. Single Bunch Instability

Keil-Schnell limit for longitudinal microwave instability is [5]

$$\left|\frac{Z_0^{\|}}{n}\right| < \frac{|\eta|E_0}{e\beta^2 I_{\rm pk}}\left[\frac{\Delta E}{E_0}\right]^2_{\rm FWHM} F_{\|}\ , \tag{4.4}$$

where I_{pk} is the peak current, η is the slip factor, E_0 is the nominal beam energy, and the energy spread ΔE at FWHM is computed according to a parabolic distribution and the

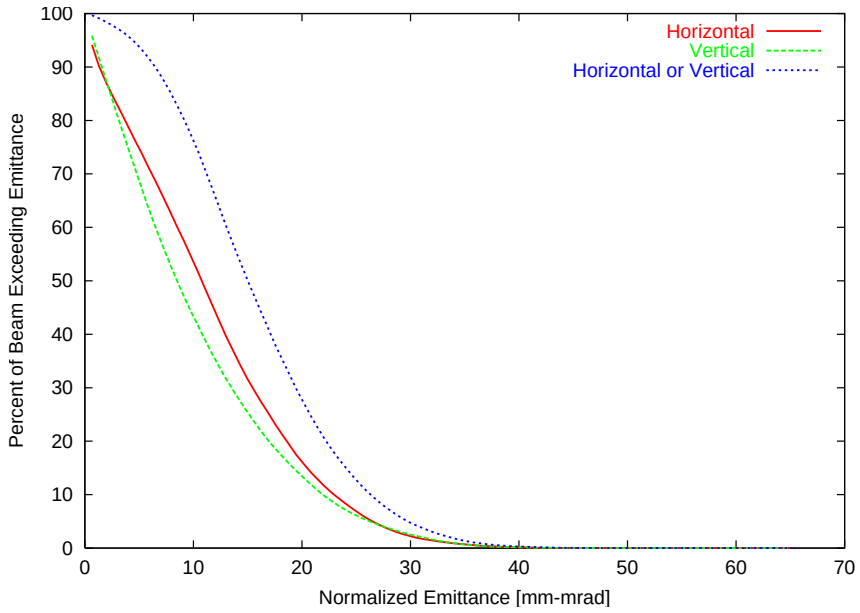

Figure 4.4. Plot showing the fractional number of particles falling outside a particular normalized emittance. The lowest curve is for vertical consideration only, the middle is for horizontal consideration only, and the uppermost one is regardless of vertical or horizontal.

form factor $F_{\|}$ is near unity for the real and inductive parts of the impedance, but is large for the capacitive part of the impedance. The stability limit is depicted in Fig. 4.5. Alongside, is also shown the space charge impedance of the beam inside the rectangular beam pipe,

$$\frac{Z_0^{\|}}{n} = i\frac{Z_0}{2\beta\gamma^2}\left[1 + 2\ln\left(\frac{4h}{\pi a}\tanh\frac{\pi w}{2h}\right)\right] , \tag{4.5}$$

where $Z_0 \approx 377\ \Omega$ is the free-space impedance and a is the beam radius.

The longitudinal resistive-wall impedance is

$$Z_0^{\|}\Big|_{\rm wall} = [1 - i\,{\rm sgn}(\omega)]\,\frac{\rho R}{h\delta_s}F_{\|}^{\rm wall} , \tag{4.6}$$

where $\delta_{\rm skin}$ is the skin depth for resistivity ρ and $F_{\|}^{\rm wall} = 0.92698$ is a form factor which takes care of the fact that the beam pipe cross section is rectangular. The beam pipe will be constructed using Inconel with $\rho = 1.29 \times 10^{-6}\ \Omega$m. The real or imaginary part of the resistive-wall impedance amounts to $2.5\ \Omega$ at the revolution frequency. Since both the space charge and resistive-wall impedances are well below the Keil-Schnell limit, the beam should be stable against longitudinal microwave instability.

The Keil-Schnell-like limit for transverse microwave instability is [6]

$$|Z_1^{x,y}| < \frac{4\nu_{x,y}E_0}{e\beta RI_{\rm pk}}\left[\frac{\Delta E}{E_0}\right]_{\rm FWHM}|S_{x,y}|F_{x,y} , \tag{4.7}$$

where the *effective chromaticity* is $S_{x,y} = \xi_{x,y} + (\hat{n} - [\nu_{x,y}])\eta$, with $\xi_{x,y}$ the chromaticity, $\hat{n} = n + \nu_{x,y}^I$, n a revolution harmonic, $\nu_{x,y}^I$ and $[\nu_{x,y}]$ the integral and decimal parts of the

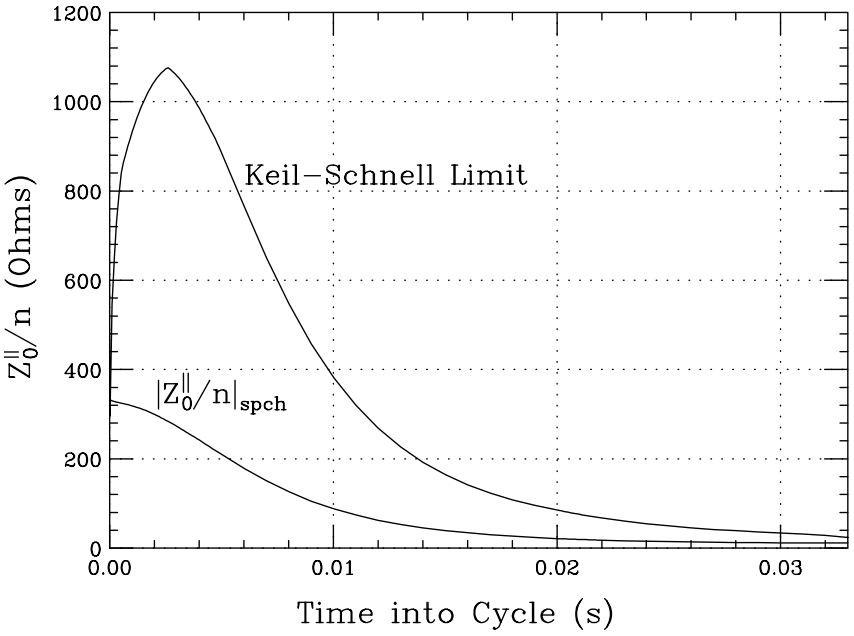

Figure 4.5. Keil-Schnell limits of longitudinal microwave instabilities for the PD2.

betatron tune. Instability occurs only for *slow waves* when $\hat{n} > [\nu_{x,y}]$. The form factor $F_{x,y}$ depends on the transverse particle distribution, about unity for the real part of the impedance but is large compared to unity for a space charge dominated impedance. Since this is a coasting-beam theory, it is applicable only when the wavelength of the perturbation is much less than twice the total bunch length. In the ramp cycle of this machine, the half bunch length is $\hat{\tau} \lesssim 5$ ns soon after adiabatic capture. Thus, the perturbation must have frequency larger than 50 MHz or revolution harmonic $n \gtrsim 100$. The slip factor η changes from -0.3668 at injection to -0.0058 at extraction (using $\gamma_t = 13.82$). The chromaticities will be negative both horizontally and vertically indicating that $S_{x,y}$ will not vanish. At injection, $S_{x,y} \approx 30$ is dominated by the slip-factor part. Near the end of the ramp, however, $S_{x,y}$ can be dominated by the chromaticity if the perturbation wavelength is as small as the bunch length. In other words, we should not expect $S_{x,y}$ to help much in the stability limit of Eq. (4.7). With $F_{x,y}|S_{x,y}| = 1$, the stability limits are depicted in Fig. 4.6. We see that, from injection to extraction, $|Z_1^y| < 0.31$ to $0.73\ \mathrm{M\Omega/m}$ $|Z_1^x| < 0.49$ to $1.20\ \mathrm{M\Omega/m}$.

The transverse resistive-wall impedance is

$$Z_1^{x,y}\Big|_{\rm wall} = \frac{2c}{h^2\omega} Z_0^{\parallel}\Big|_{\rm wall} \frac{F_{x,y}^{\rm wall}}{F_x^{\rm wall}}\ , \tag{4.8}$$

with the form factors $F_x^{\rm wall} = 0.40825$ and $F_y^{\rm wall} = 0.81979$, leading to $|Z_1^y| = 0.07\ \mathrm{M\Omega/m}$ and $|Z_1^x| = 0.14\ \mathrm{M\Omega/m}$ at the revolution frequency. These are small compared with Eq. (4.7). On the other hand, the space charge contributions are $Z_1^y = i54$ to $i7.3\ \mathrm{M\Omega/m}$ and $Z_1^x = i70$ to $i7.6\ \mathrm{M\Omega/m}$ from injection to extraction, much larger than the limits quoted in Eq. (4.7). However, reactive impedance will not lead to instability if the resistive part can be controlled.

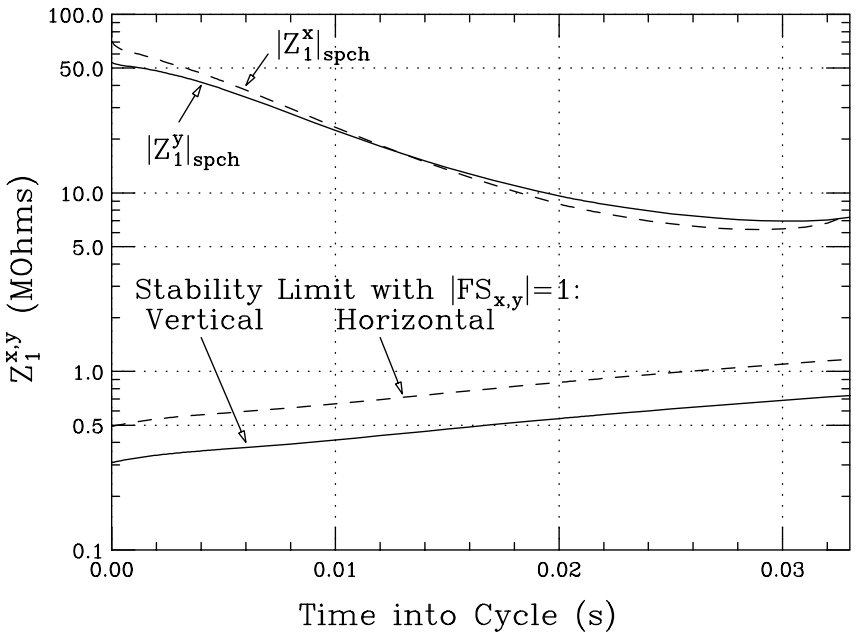

Figure 4.6. Keil-Schnell-like limits of transverse microwave instabilities for the PD2.

4.1.4. Coupled-bunch Instability

The resistive-wall impedance can drive transverse coupled-bunch instability with a growth rate

$$\frac{1}{\tau_\mu^{x,y}} \approx \frac{eMI_b c}{4\pi\nu_{x,y}E_0}\,\mathcal{R}e\,Z_1^{x,y}(\nu_{x,y}^c\omega_0)F\ , \tag{4.9}$$

where the form factor is $F \sim 0.811$ if sinusoidal modes are assumed and the instability is worst at injection. For $\nu_y = 7.34$, $[\nu_y] = 0.34$, $\nu_{x,y}^c = [\nu_{x,y}] - 1 = -0.66$ and $\mathcal{R}e\,Z_1^{x,y}(\nu_y^c\omega_0) = -0.088$ MΩ/m. The growth rate is $302\ \mathrm{s}^{-1}$ or growth time 3.30 ms or 1660 turns. This instability is hard to damp with chromaticity since $|\eta| = 0.3668$ at injection is not small. For example, with $\xi_y = -20$ and full bunch length $\tau_L = 10$ ns, $\omega_\xi\tau_L/\pi = 2f_0\xi_y\tau_L/|\eta| = 0.55$ and the form factor is reduced by only $\sim 5\%$. To damp this instability, one may need octupoles and/or a mode damper.

Coupled-bunch instabilities, longitudinal or transverse, driven by the higher-order modes of the rf cavities are quite different. This is because resonances from cavities have fixed frequencies. Since revolution frequency changes fast during ramping, these resonances will move through the revolution harmonics. In other words, a coupled-mode is driven for only a short time. Thus there will not be any growth at the early part of the cycle. For the driving frequency $f_r = \omega_r/(2\pi)$, define the resonant harmonic $n_r = f_r/(\beta f_\infty)$ where $f_\infty = c/(2\pi R)$. The drift rate at the harmonic n_r is $\dot{\beta}n_r f_\infty$. The time required to drift through the HWHM of the resonance with quality factor Q is

$$\Delta t = \frac{2\beta}{\dot{\beta}Q} = \frac{2\gamma^3\beta^2}{Q\dot{\gamma}}\ , \tag{4.10}$$

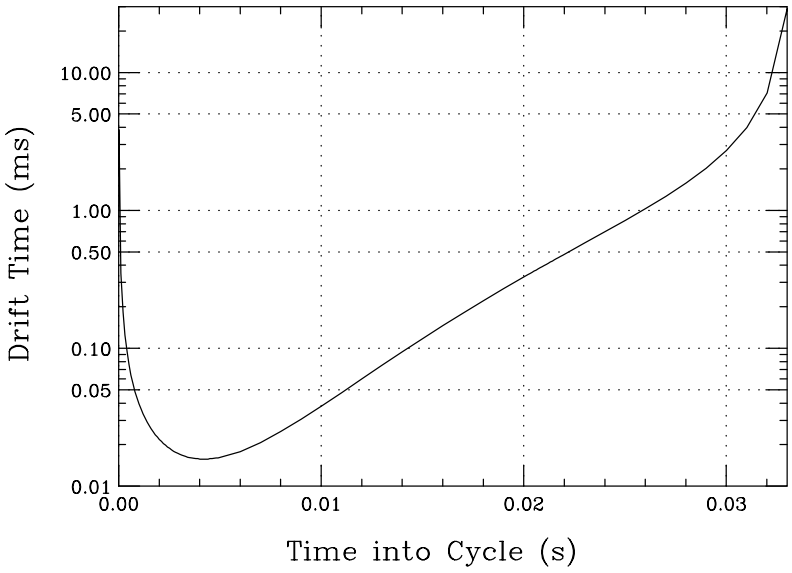

Figure 4.7. Time for a higher-order resonance of fixed frequency to drift through a harmonic line of the PD2.

implying that any coupled-bunch growth time $\gtrsim \Delta t$ cannot materialize. This is plotted in Fig. 4.7 for the situation of $Q = 5000$. Any coupled-bunch instabilities that occur during the latter part of the cycle will have similar behavior as those observed in the present booster; of course the growth rate will be faster. At this part of the cycle, the energy of the beam is much larger making the growth rates smaller. Since these couplings occur at high frequencies, the form factor drops as the bunch length increases; for example, at angular driving frequency ω_r, $F \sim e^{-(\omega_r \sigma_\tau)^2}$ for a Gaussian distribution with rms bunch length σ_τ.

4.2. Longitudinal Dynamics

James MacLachlan

The rf systems and longitudinal dynamics of the 8 GeV Proton Driver (PD2) relate most closely to the Phase I, Stage 1 description of the previous Proton Driver Design Study. Because of the smaller size and drastic change in lattice for the 8 GeV machine, however, few specific parameters carry over. Nonetheless, the design concepts are similar. The present study is like an addendum to the PD1 Design Study; what follows builds on Ch. 5. In common with the previous design, modified Booster cavities and a 15 Hz sinusoidal magnet ramp with a second harmonic are used. The usefulness of an inductive insert for space charge compensation remains an attractive but less crucial speculation. The parameters governing the longitudinal dynamics are summarized in Table 4.1.

Proton Driver 2 is fundamentally a high intensity injector or super booster for the MI. Accordingly, the use of modified Booster rf cavities is much less of a limitation than for

Table 4.1. 8 GeV Proton Driver specifications important for the rf design.

$E_{\rm inj}$	injection kinetic energy	600	MeV
	beam intensity	2.5×10^{13}	p/cycle
	cycle repetition rate	15	Hz
$E_{\rm ext}$	extraction kinetic energy	8	GeV
$R_{\rm eq}$	mean radius of equilibrium orbit	75.471	m
$f_{\rm rf}$	accelerating cavity frequency	42 – 53	MHz
h	harmonic number	84	
	number of populated buckets (at extraction)	81	
$\hat{V_{\rm rf}}$	maximum rf voltage	1.05	MV
	number of rf cavities	20	
ε_ℓ	95 % norm. longitudinal emittance (at extraction)	0.2	eVs
	bunch intensity	3×10^{11}	
	rms bunch length (at extraction)	1	ns
$\Delta E_{\rm inj}$	energy spread at injection	± 0.25	MeV
$\alpha_\circ$	momentum compaction	5.251×10^{-3}	
α_1	coefficient of $(\Delta p)^2$ in path length	-8.46×10^{-3}	
g	geometric factor for space charge	2.05	
$Z_\parallel/n$	high frequency broadband longitudinal impedance (estimate)	2	Ohm
	momentum acceptance	$\pm 1\%$	

the Phase 1, Stage 1 of the previous proposal. For example, a pure sinusoidal ramp is a cost saving option if the cavity count can be raised from 20 to 22. Also, inductive inserts are not necessary to achieve low losses.

Losses and emittance growth have been evaluated for three ramp options, a pure sinusoidal ramp like the present Booster and two using 12.5 % addition of second harmonic to reduce the maximum $\dot{p}$ (rate of change of momentum). One variant minimizes $\dot{p}$ early in the cycle; it is called here a "minimum $\dot{p}$ ramp" although partly it postpones the peak $\dot{p}$. The ramp which is called "minimum rf power" has a higher slope early in the cycle where the rf voltage is limited by tuner performance but has a lower maximum rf power. The $\dot{p}$ curves are plotted in Fig.4.8. In every case the maximum rf voltage has been limited to 1.05 MV; the twenty modified Booster cavities are expected to make this voltage, but the current capability is marginal for a pure sine ramp. Additional cavities are desirable to provide for reliable, stable operation.

The capture phase of the cycle is common to the three ramp variants. It has been optimized with perfectly conducting wall space charge taken into account with no other source of longitudinal impedance. Given that generally other $Z_\parallel$ is likely to have an inductive component, this condition is probably worst case for capture. Very small reduction in rf voltage in the first 5 ms produces significant losses; so the voltage specified includes little or no safety margin for operational variability. Practically some margin will be needed; if studies establish that an inductive insert is otherwise benign, a substantial safety margin for capture can be obtained inexpensively in this way. However, it is also possible that the modified cavities will provide sufficient voltage to cover reasonable operational variability. Failing positive results on both inductive insert and cavity gradient, another pair of cavities would be prudent.

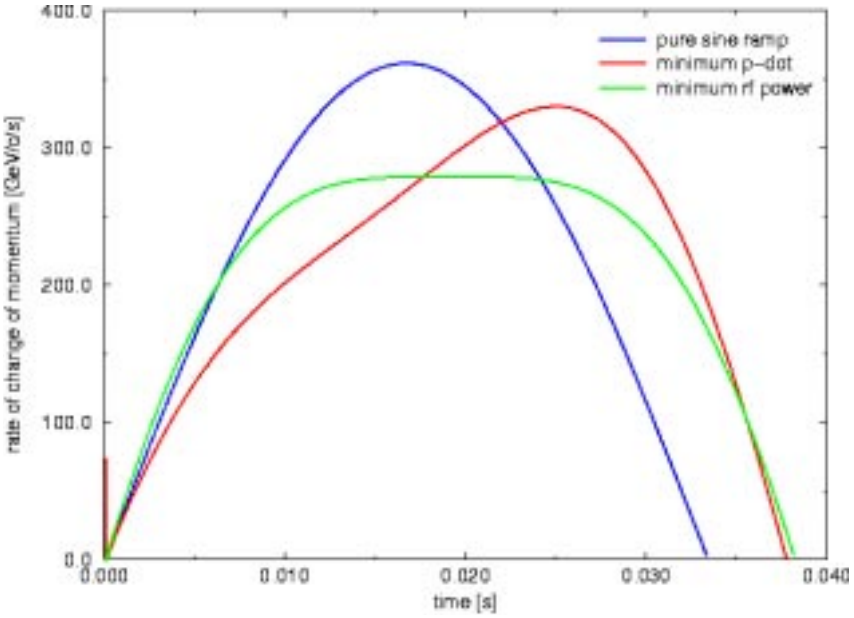

Figure 4.8. (color) Rate of change of momentum $\dot{p}$ [GeV/c/s] *vs.* time [s] for three ramp variants: pure sinusoidal ramp, ramp with second 12.5 % second harmonic phased for least $\dot{p}_{\max}$, ramp with 12.5 % second harmonic phased for least peak rf power.

Table 4.2 summarizes the basic results. Any of the quoted losses and final emittances would be acceptable if actually achieved, but the modeling is too idealized to support such an expectation. Rather one notes by comparison such details as the the tendency of the minimum rf power ramp toward higher loss because of faster ramp early in the cycle. Despite the clear appeal of the minimum rf power ramp, in an optimized design a different choice might be made based on a detailed tradeoff on RF power required and the frequency at which the peak power is required. Postponing the higher slope until later in the cycle may turn out to be beneficial because of better tuner performance at higher frequency. The rms and 95 % emittances at extraction don't appear to correlate closely. The rms values are more solid because the 95 % values are disproportionately affected by scraping with whatever loss there is and furthermore are not evaluated very precisely. However, all of the 95 % values have better than ten percent precision and exceed the Table 4.1 specification.

With respect to anticipated instabilities, the considerations of the PD1 Design Study

Table 4.2. Performance on variant ramps.

Ramp type →	sine ramp	minimum $\dot{p}$	min. rf power
max. rate of momentum change [GeV/c/s]	361.4	329.9	278.8
accelerating voltage at $\dot{p}_{\max}$ [MV]	0.93	0.78	0.99
synchronous phase at $\dot{p}_{\max}$ [deg]	38	42	26
rf accelerating power at $\dot{p}_{\max}$ [MW]	1.4	1.3	1.1
95% longitudinal emittance at extraction [eVs]	0.07	0.10	0.08
rms longitudinal emittance at extraction [eVs]	0.0078	0.0077	0.0107
loss (all below 1.2 GeV)	< 0.1 %	0.0	0.6 %
loss with inductive insert	0.0 %	0.0 %	0.0 %

remain generally relevant; however, the design beam current is 25 % higher because of the reduced circumference even though the number of protons has been reduced by 17 %. Controlling longitudinal coupled bunch instability will require not only a concerted effort on higher order mode suppression in the cavities but at least some level of active damping.

4.2.1. Extraction and Bunch rotation

The longitudinal matching of PD2 to the MI is practically the same as for the current Booster-MI transfer. About 90 kV in the PD matches a 0.8 eVs bucket generated by 1 MV or so in the MI. This bucket sounds a bit large, but it can not be reduced by much and still provide control and acceptable bucket shape distortion; it can be reduced a little if desired on the MI ramp.

Bunch rotation is not so important in PD2 as it was for the original Proton Driver design for two reasons. First of all, the momentum acceptance of the PD2 ring is only 40 % of the original, so path length dependence on momentum is less serious. It is accounted for to the first order correction in $\Delta p/p$. On the other hand, with advertised dynamic aperture of 250 π, path length dependence on betatron amplitude may be significant. This has not been accounted for in either study. Bunch rotation is also less important programmatically in the absence of a neutrino factory or μ storage ring. Neutrino beam users might make good use of tighter timing for gating and TOF discrimination. The result of a rotation on the ramp is shown in Fig. 4.9; the nonlinearity of the rotation is evident in the C-shaped bunch instead of the classic S and also in the up-down asymmetry of the bucket. However, the rms bunch width is only 0.2 ns with the rather reasonable symmetry about the mean shown in Fig. 4.10.

References

[1] L.J. Laslett, Proceedings of 1963 summer Study on Storage Rings, BNL-Report 7534, p. 324.

[2] F. Sacherer, *Transverse Space Charge Effect in Circular Accelerators*, Lawrence Rad. Lab. UCRL-18454 (PhD Thesis, University of California, 1968).

[3] C. Prior, Track-2D, private communication.

[4] J. Holmes, private communication.

[5] E. Keil and W. Schnell, CERN Report TH-RF/69-48 (1969); V.K. Neil and A.M. Sessler, Rev. Sci. Instr. **36**, 429 (1965).

[6] B. Zotter and F. Sacherer, *Transverse Instabilities of Relativistic Particle Beams in Accelerators and Storage Rings*, Proceedings of the First Course of the International School of Particle Accelerators of 'Ettore Majorana' Centre for Scientific Culture, Erice 10-22 November 1976, p. 175.

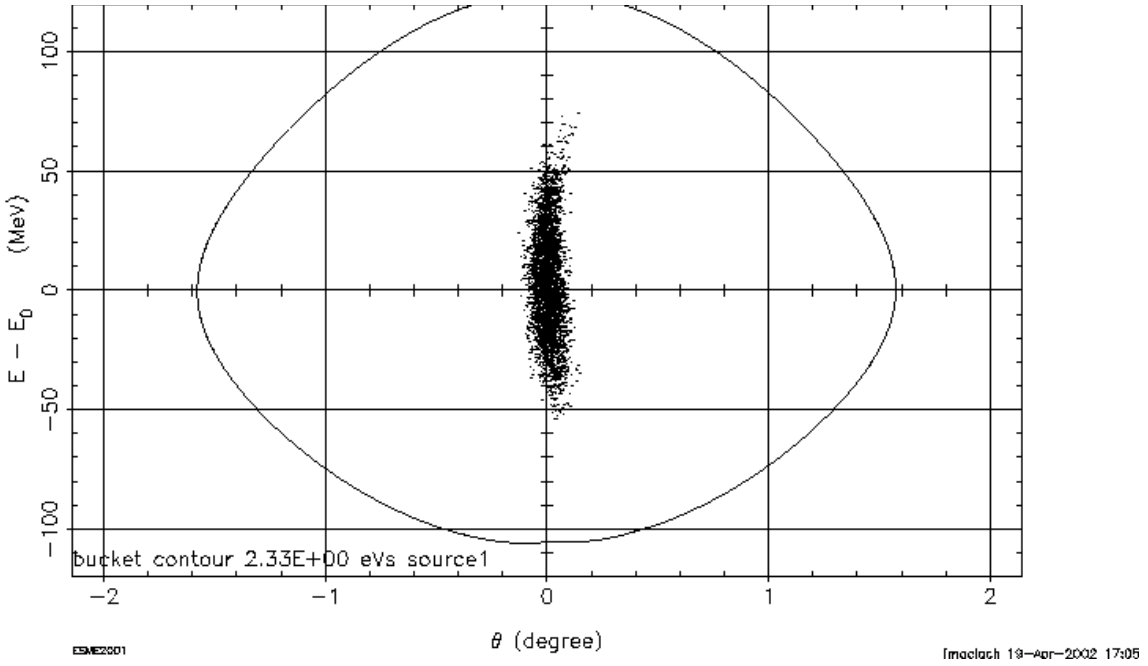

Figure 4.9. The phase space distribution of a bunch rotated with 1 MV of rf at the end of the minimum $\dot{p}$ ramp. The horizontal axis on this plot is just under 19 ns long; the units are $h = 1$ phase in degrees and energy in MeV. The momentum spread is about ± 0.8 %.

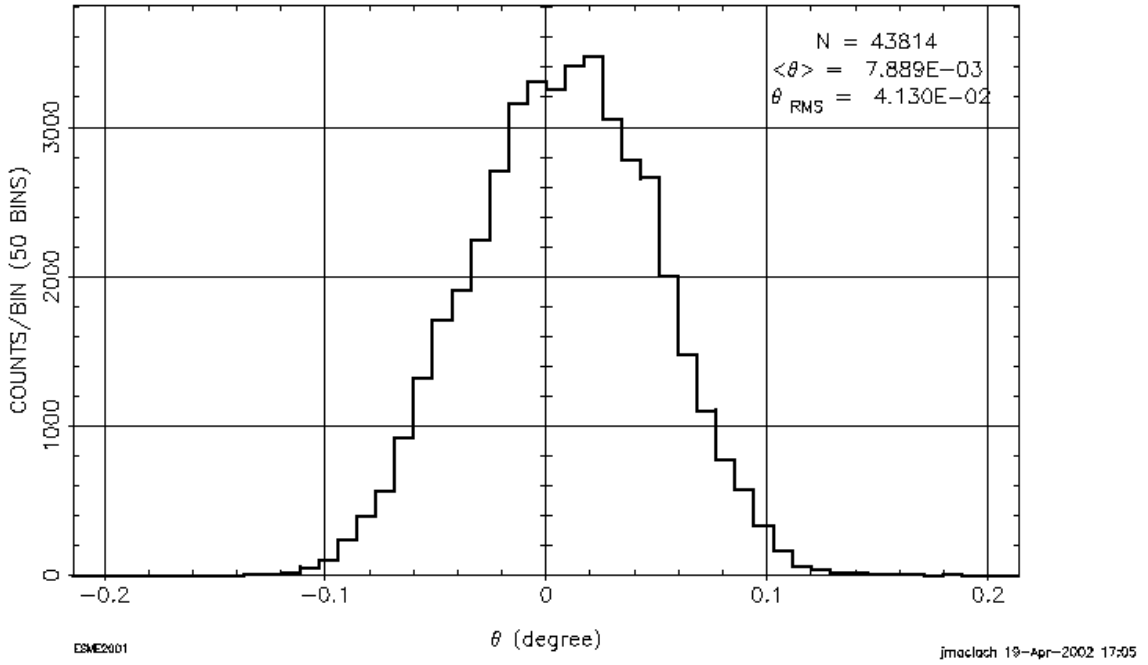

Figure 4.10. The bunch length profile plotted against h=1 phase in degrees; the horizontal axis corresponds to 1.9 ns.